Predicting Fluid Flow Regime, Permeability, and Diffusivity in Mudrocks from Multiscale Pore Characterisation

Amirsaman Rezaeyan[1*], Vitaliy Pipich[2], Jingsheng Ma[3], Leon Leu[4], Timo Seemann[5], Gernot Rother[6], Lester C. Barnsley[2,7], and Andreas Busch[1]

[1] Lyell Centre, Institute of GeoEnergy Engineering, Heriot-Watt University, Edinburgh, EH14 4AS, UK

[2] Forschungszentrum Jülich GmbH, Jülich Centre for Neutron Science JCNS at Heinz Maier-Leibnitz Zentrum MLZ, Garching, 85748, Germany

[3] Institute of GeoEnergy Engineering, Heriot-Watt University, Edinburgh, EH14 4AS, UK

[4] Department of Earth Science and Engineering, Imperial College London, London, SW7 2AZ, UK

[5] Clay and Interface Mineralogy, RWTH Aachen University, Aachen, 52072, Germany

[6] Chemical Sciences Division, Oak Ridge National Laboratory, Oak Ridge, TN, 37922, USA

[7] Australian Synchrotron, ANSTO, Clayton, 3168, Australia

*Corresponding author: Amirsaman Rezaeyan (ar104@hw.ac.uk; amirsaman.rezaeyan@gmail.com)

Key Points:

- Small angle neutron scattering data provides input for fractal permeability and diffusivity modelling in mudrocks.
- Fluid flow predictions in mudrocks are pore size dependent.
- Integration of pore-size dependent fluid flow regimes in modelling and simulation studies can help prediction of transport properties (permeability and diffusivity) in mudrocks.

Abstract

In geoenergy applications, mudrocks prevent fluids to leak from temporary (H_2, CH_4) or permanent (CO_2, radioactive waste) storage/disposal sites and serve as a source and reservoir for unconventional oil and gas. Understanding transport properties integrated with dominant fluid flow mechanisms in mudrocks is essential to better predict the performance of mudrocks within these applications. In this study, small-angle neutron scattering (SANS) experiments were conducted on 71 samples from 13 different sets of mudrocks across the globe to capture the pore structure of nearly the full pore size spectrum (2nm-5μm). We develop fractal models to predict transport properties (permeability and diffusivity) based on the SANS-derived pore size distributions. The results indicate that transport phenomena in mudrocks are intrinsically pore size dependent. Depending on hydrostatic pore pressures, transition flow develops in micropores, slip flow in meso- and macropores, and continuum flow in larger macropores. Fluid flow regimes progress towards larger pore sizes during reservoir depletion or smaller pore sizes during fluid storage, so when pressure is decreased or increased, respectively. Capturing the heterogeneity of mudrocks by considering fractal dimension and tortuosity fractal dimension for defined pore size ranges, fractal models integrate apparent permeability with slip flow, Darcy permeability with continuum flow, and gas diffusivity with diffusion flow in the matrix. This new model of pore size dependent transport and integrated transport properties using fractal models yields a systematic approach that can also inform multiscale multi-physics models to better understand fluid flow and transport phenomena in mudrocks on the reservoir and basin scale.

1 Introduction

Technologies utilising the subsurface are impacted by the presence and properties of mudrocks. This includes the energy industry evaluating top seals for hydrocarbons or the properties of shale gas reservoirs, but also applications relating to the energy transition like permanent storage of CO_2, or intermittent storage of H_2 or CH_4 (Amann-Hildenbrand et al., 2013; Beckingham and Winningham, 2020; Busch and Kampman, 2018; Ilgen et al., 2017). In addition, mudrocks have been identified as a potential host rock for the disposal of radioactive waste, where H_2 can be generated from anoxic corrosion of stainless-steel waste containers and from water radiolysis reactions caused by alpha decay (Charlet et al., 2017; Sellin and Leupin,

2013). To assess the feasibility of mudrocks for these (geo)technical applications, it is necessary to characterise their pore structures (Bustin et al., 2008; Rutter et al., 2017). The study of porosity in mudrocks has improved through the (combined) application of standard to advanced techniques, such as fluid immersion, gas adsorption, mercury intrusion porosimetry, electron microscopy, nuclear magnetic resonance, or X-ray and neutron scattering (Anovitz and Cole, 2015; Busch et al., 2016; 2017; Leu et al., 2016). However, our understanding of how fluid flow regimes and transport properties (e.g. permeability and diffusivity) are controlled by the pore structure in mudrocks across different scales is limited. The pore structure of mudrocks consists of inter- and intra-particle pore space related to organic and inorganic matrix components (Chalmers et al., 2012; Curtis et al., 2010; Loucks et al., 2012; Nelson, 2009). Pore sizes generally range over several orders of magnitude, including macropores > 50 nm, mesopores 2-50 nm, and micropores < 2 nm according to the International Union of Pure and Applied Chemistry (IUPAC) pore size classification (Sing et al., 1985).

Intrinsic permeability is a function of topology and morphology of pores (Day-Stirrat et al., 2011; Kuila et al., 2014; Loucks et al., 2009), even though the permeability in mudrocks is also stress dependent (Cui et al., 2009). In addition to traditional Hagen–Poiseuille or Darcy type viscous flow descriptions, slip flow governs transport phenomena in mudrocks that encompass pores from macrometer to micrometer scales (Amann-Hildenbrand et al., 2012; Gensterblum et al., 2015; Ilgen et al., 2017; Sakhaee-Pour and Bryant, 2012). It has been shown that transport in mudrocks varies at different characteristic time and length scales (Amann-Hildenbrand et al., 2012; Gensterblum et al., 2015; Ghanizadeh et al., 2014b; Javadpour, 2009; Javadpour et al., 2007). In this context, the Knudsen number (K_n), defining the ratio between the molecule mean free path length and the pore size, allows characterising the pore size boundaries for fluid flow regimes (Knudsen, 1909). In fact, it relates dominant flow regimes to the corresponding range of pore sizes in the matrix: free molecular/Knudsen diffusion flow (K_n>10), transitional flow (0.1<K_n<10), slip flow (0.001<K_n<0.1), and continuum/Darcy flow (K_n<0.001) (Colin, 2014; Tartakovsky and Dentz, 2019). The pore structure of mudrocks accommodates the rock-fluid interactions controlling transport of elements associated with hierarchical pore morphology (Bahadur et al., 2014; Busch et al., 2017). This leads to a scale dependence of effective permeability, which brings about different fluid flow mechanisms at the corresponding pore size (Amann-Hildenbrand et al., 2012; Mehmani et al., 2013).

In this study, we developed fractal models to predict permeability and diffusivity for dominant fluid flow regimes. This novel systematic approach will be capable of informing (upscaled) multiscale, multi-physics models dealing with geochemical and hydraulic processes in mudrocks on the reservoir and basin scale. For characterisation of the full pore size range of mudrocks we employ a combination of very small-angle neutron scattering (VSANS) and small-angle neutron scattering (SANS) to quantitatively capture the pore characteristics of a wide range of organic lean and organic rich mudrocks from multiple global locations. This SANS-driven multiscale characterisation, covering pore sizes from 2 nm to 5 µm, includes fractal dimensions, specific surface area (SSA), porosity, and pore size distribution (PSD). We show how different fluid flow regimes are controlled by different pore size ranges at different reservoir depths and how they are related to porosity. Model outputs are matched with fluid flow experiments performed on plug samples and provide an improved understanding of permeability and diffusion in mudrocks to inform caprock leakage or unconventional reservoir production.

2 Materials and Methods

2.1 Samples

Experimental work to characterise the pore structure was carried out on two groups of mudrocks, with the first group consisting of 40 organic lean and the second group of 31 organic rich samples. The mudrocks studied differ in lithology, mineralogy, age, depositional environment, and burial depth (Table 1).

Table 1. Overview of the sample sets used in this study. Full details of samples are available in Supporting Information (S1).

Type	Mudrock Name	Main Minerals	Depositional Environment, Age, and maximum Burial Depth	Application	Location	Geological Details
Organic Lean Mudrocks	Opalinus Clay	quartz, illite, and kaolinite	marine; Carboniferous; 1800m	potential host rock for the disposal of radioactive waste	Mont Terri, Switzerland	Bossart and Thury (2008), Mazurek et al. (2002)

	Boom Clay	quartz, illite, and montmorillonite	marine; Oligocene; 400m	potential host rock for the disposal of radioactive waste	Mol, Belgium	Bruggeman and Craen (2012); Vandenberghe et al. (2014)
	Våle Shale	quartz, calcite, illite, and montmorillonite	marine; Paleocene; 3000m	hydrocarbon seal	Møre, Norway	Gjelberg et al. (2005), Möller et al. (2004)
	Carmel Claystone / Big Hole	dolomite and illite / quartz, k-feldspar, dolomite, and illite	marine; Jurassic; 2200m	seal for natural CO_2 reservoir	Utah, USA	Blakey et al. (1996), Petrie et al. (2014)
	Entrada Siltstone	quartz, dolomite and illite	marine; Jurassic; 2200m	seal for natural CO_2 reservoir	Utah, USA	Johansen and Fossen (2008), Kampman (2011)
Organic Rich Mudrocks (Gas Shales)	Posidonia Shale	quartz, calcite, pyrite, kaolinite, and illite	marine; variable: from Jurassic/ Cretaceous; 7800m	hydrocarbon source rock	Northern Germany	Bruns et al. (2016); Klaver (2014); Schlosser et al. (2016)
	Carboniferous Shale	quartz, siderite, kaolinite, and illite	terrestrial; Carboniferous; 5640m	black shale	North-east Belgium	Vandewijngaerde et al. (2016), Uffmann et al. (2012)
	Bossier Shale	quartz, k-feldspar, calcite, and illite	marine; Jurassic/ Cretaceous; 9335m	black shale	Louisiana, USA	Hammes and Frébourg (2012), Klaver et al. (2015)
	Haynesville Shale	quartz, calcite, and illite	marine; Jurassic; 9975m	black shale	Louisiana and Texas, USA	Hammes and Frébourg (2012), Klaver et al. (2015)
	Eagle Ford Shale	Quartz, calcite, kaolinite, and illite	marine; Cretaceous; 6500m	black shale	Texas, USA	Dawson and Almon (2010), Pearson (2012)
	Jordan Shale	quartz, calcite, and illite	marine; Cretaceous; 4200m	black shale	Jordan	Amireh (1997)
	Newark Shale	quartz, ankerite, and illite	lacustrine; Triassic; 9850m	black shale	New Jersey, USA	Olsen et al. (1996), Fink et al. (2018)

2.2 Mineralogy and Geochemistry

Bulk mineralogical compositions were derived from X-ray diffraction patterns of randomly oriented powder preparates of Opalinus, Carmel, Entrada, Posidonia, Carboniferous, Bossier, Haynesville, Eagle Ford, Newark, and Jordan samples on a Bruker D8 diffractometer using CuKα-radiation produced at 40kV and 40mA. The mineralogy of Boom samples was obtained from Jacops et al. (2017), mineralogy of Våle shale samples was kindly provided by Norske Shell, Norway. Total organic carbon (TOC) content data were measured on powdered samples with a LECO RC-412 Multiphase Carbon/Hydrogen/Moisture Determinator. Vitrinite reflectance (VR_r) data were obtained using oil immersion (ne=1.518) on a Zeiss Axio Imager microscope. Details of the mineralogical and geochemical compositions of the mudrocks and details of the measurements are provided in Supporting Information (S2.1 and S2.2).

2.3 Very Small- and Small-Angle Neutron Scattering Experiments

VSANS and SANS experiments at ambient pressure and temperature conditions were conducted at the FRM-II facility at the Heinz Maier-Leibnitz Zentrum (MLZ) in Garching, Germany. Air-dried mudrock samples were cut parallel to bedding, fixed on quartz glass slides, and polished to a thickness of ~ 0.2 mm. SANS measures the scattering intensity I(Q) as a function of momentum transfer Q, the resulting scattering curves contain statistical information that allows pore structure interpretations based on a shape model e.g., the polydisperse spherical (PDSP) model (Melnichenko, 2015). We used the KWS-3 instrument, operated by the Jülich Centre for Neutron Science (JCNS) at MLZ, to obtain very small angle neutron scattering (VSANS) data of all samples, which detects pore sizes of ca. 5 µm – 250 nm. Data at KWS-3 were collected at wavelength of λ =12.8 Å (with a wavelength distribution of the velocity selector $\Delta\lambda/\lambda$ = 0.2), and a sample-to-detector distance of 9.5 m, covering a Q-range from 0.0024 to 0.00016 $Å^{-1}$ (Pipich and Fu, 2015). SANS data was obtained using the KWS-1 instrument, operated by the JCNS at MLZ, covering pore sizes between 250 nm – 1 nm. Measurements at KWS-1 were performed using wavelengths λ = 5 and λ = 7 Å with a 10% spread at sample-to-detector distances of 1.2, 7.7, and 19.7 m, covering a Q-range of 0.002 – 0.35 $Å^{-1}$ (Feoktystov et al., 2015; Frielinghaus et al., 2015). Data correction, normalisation, radial averaging, and background subtraction were carried out using the QtiKWS software (Pipich, 2006), following standard procedures of the instruments. The data processing and analysis were carried out using

our MATSAS software (Rezaeyan et al., 2021). The analysis of scattering profile yields fractal dimensions, specific surface area (SSA), porosity, and pore size distribution. Full experimental and analytical information are provided in Supporting Information (S2.3).

3 Fractal Models

Mudrocks are often characterised by a fractal geometry (Liu and Ostadhassan, 2017; Radlinski et al., 1996; Zhang et al., 2017); a detailed discussion is available in Radlinski (2006). The geometry of pores in nature can be described by the single number D_f, the fractal dimension, representing pores are self-similar but over a limited pore size range (Teixeira, 1988; Wong et al., 1986). The deviation from self-similarity across scales can be due to variations in essential mineral constituents e.g., clay minerals, see Krohn (1988) for further discussions. Mudrocks are foliated, which is why the sample thickness should be as thin as its constituting clayey lamina to satisfy self-similarity. However, one lamina-thick sample does not provide adequate statistical information for adequate pore structure interpretations. Therefore, we argue a trade-off for the sample thickness (~ 200 µm) must be considered to allow for a sufficient Q-range for measuring the relevant slope (m), thereby D_f. Given that fractal dimensions provide morphological information on the surface roughness of pore networks, fractal models can be used to predict the matrix permeability (Miao et al., 2015; Yu and Cheng, 2002) as well as diffusivity (Busch et al., 2018; Liu and Nie, 2001; Zheng et al., 2018). Based on the pore structure information obtained from SANS, we developed three fractal models to predict: (i) Darcy permeability for continuum flow, (ii) apparent permeability for slip flow regimes and (iii) effective diffusion (diffusivity) for diffusional flow regimes in mudrocks.

3.1 Permeability Fractal Models

The fluid pathways of mudrocks are associated with (micro)-fractures as well as matrix-hosted pore bodies and throats associated with inorganic and organic compounds (Ghanizadeh et al., 2014b). Depending on the dominant fluid flow regime, the matrix permeability is subdivided into two main categories: Darcy permeability (no slip-flow boundary condition; K_n<0.001) and apparent permeability (slip flow boundary condition; 0.001<K_n<0.1) (Javadpour, 2009). We developed analytical fractal solutions that relate permeability to three pore characteristics including fractal dimension (D_f), tortuosity fractal dimension (D_τ), and porosity (φ) associated

with a dominant pore size χ which ranges between χ_{min} and χ_{max}. The fractal model to predict Darcy permeability is based on the Hagen–Poiseuille equation representing flow in a unit cell consisting of a bundle of tortuous capillary tubes with circular cross-sectional area and a fractal distribution of pore sizes (Yu and Cheng, 2002); the relationship between pore size and pore number can be described using the general power scaling law leading to fractal dimension (Katz and Thompson, 1985; Mildner and Hall, 1986):

$$N(\geq \chi) = \left(\frac{\chi_{max}}{\chi}\right)^{m} = \left(\frac{\chi_{max}}{\chi}\right)^{6-D_f} \quad (1)$$

where N is the cumulative number of capillary tubes $\geq \chi$, $m = 6 - D_f$ is the slope of the pore density distribution directly obtained from the neutron scattering profile (Radlinski, 2006). Yu and Cheng (2002) suggest using the first derivative of the fractal distribution function between χ_{min} and χ_{max}. Therefore, the number of capillary tubes between χ and $\chi + d\chi$ can be derived by differentiating Equation (1):

$$-dN(\chi) = \left(6 - D_f\right)\chi_{max}^{6-D_f}\chi^{D_f-7} \quad (2)$$

The negative sign in Equation (2) implies that the density of capillary tubes decreases with an increase in pore size, and $-dN(\chi) > 0$ (Yu and Cheng, 2002). In addition to the pore size of capillary tubes, the tortuous pathways have fractal characteristics. Yu and Cheng (2002) argued that the connection between the tortuous capillary size and its length satisfy the same fractal scaling law; this has been verified for sandstone (Chen and Yao, 2017), carbonates (Wang et al., 2019) and shales (Sheng et al., 2016; Zhang et al., 2018). Using a modification by Wheatcraft and Tyler (1988), the quantitative relationship between pore size and pore length within a bundle of capillaries is described as

$$\frac{L(\chi)}{L_0} = \left(\frac{L_0}{\chi}\right)^{6-D_\tau} \quad (3)$$

and

$$L(\chi) = {L_0}^{7-D_\tau}\,\chi^{D_\tau-6} \quad (4)$$

where L_0 (tortuosity $\tau = 1$) and $L(\chi)$ (tortuosity $\tau > 1$) are the straight and tortuous lengths of capillary tubes between the start and end points of the fractal path. The range of D_τ is $1<D_\tau<3$; $D_\tau = 1$ corresponds to a straight capillary and $D_\tau = 3$ represents a highly tortuous capillary in

3D (Wheatcraft and Tyler, 1988). The average tortuosity ($\bar{\tau}$) can be described as a transformation relationship between the general topological dimension (D_G) and D_τ (Wheatcraft and Tyler, 1988):

$$\bar{\tau} = \varepsilon^{D_G - D_\tau} \tag{5}$$

where ε is the ratio of L_0 to the average (mean) pore size ($\bar{\chi}$). For $D_G = 3$, the tortuous fractal dimension is thus expressed as:

$$D_\tau = 3 - \frac{\ln \bar{\tau}}{\ln \frac{L_0}{\bar{\chi}}} \tag{6}$$

where $\bar{\tau}$ is a function of porosity (φ) and calculated from Xu and Yu (2008):

$$\bar{\tau} = \frac{1}{2}\left[1 + \frac{1}{2}\sqrt{1-\varphi} + \frac{\sqrt{\left(\sqrt{1-\varphi}-1\right)^2 + \frac{1-\varphi}{4}}}{1-\sqrt{1-\varphi}}\right] \tag{7}$$

The straight capillary tube is related to the total cross area; $L_0 = \sqrt{A}$ [m], and $A = A_p/\varphi$ [m^2]. Wu and Yu (2007) propose that the total pore area (A_p) can be obtained from:

$$A_p = -\int_{\chi_{min}}^{\chi_{max}} \frac{\pi \chi^2}{4} dN \tag{8}$$

By substituting Equation (2) in Equation (8), the total cross sectional area A of a unit cell perpendicular to the flow direction is:

$$A = -\frac{\pi}{4\varphi}\frac{6-D_f}{4-D_f}\chi_{max}^2\left[1 - \left({\chi_{min}}/{\chi_{max}}\right)^{D_f-4}\right] \tag{9}$$

where $\varphi = (\chi_{min}/\chi_{max})^{2-m} = (\chi_{min}/\chi_{max})^{D_f-4}$ (Yu and Li, 2001). L_0 can be expressed as:

$$L_0 = \sqrt{\frac{\pi}{4}\frac{6-D_f}{4-D_f}\frac{1-\varphi}{\varphi}\chi_{max}^2} \tag{10}$$

Under continuum flow conditions (K_n<0.001), the pore size is significantly larger than the mean free path length of gas molecules. This results in the dominance of the molecule-molecule collisions leading to viscous Poiseuille flow. The gas flow rate through a single

tortuous capillary, $q_L(\chi)$, is given by modifying the well-known Hagen-Poiseuille equation (Cussler, 1997):

$$q_L = \frac{\pi \Delta P}{128 \mu_g} \frac{\chi^4}{L(\chi)} \tag{11}$$

where μ_g is gas viscosity [Pa.s] and ΔP is the pressure gradient [Pa]. The total gas flow rate (Q_t) [$m^3.s^{-1}$] can be obtained by integrating the individual flow rate $q_L(\chi)$ over the entire pore size range for continuum flow in a unit cell:

$$Q_t = -\int_{\chi_{min}}^{\chi_{max}} q_L(\chi) dN(\chi) \tag{12}$$

Substituting Equations (2), (4), and (11) into Equation (12), the integration gives

$$Q_t = \frac{\pi \Delta P}{128 \mu_g} \frac{6 - D_f}{D_f - D_\tau + 4} \frac{\chi_{max}^{10-D_\tau}}{L_0^{7-D_\tau}} \left[1 - \left({\chi_{min}}/{\chi_{max}}\right)^{D_f - D_\tau + 4}\right] \tag{13}$$

We assume that the maximum pore size (χ_{max}) does not exceed the length of a capillary tube (L_0), and is therefore described by a similar fractal scaling law (Yu and Cheng, 2002). As a result, the intrinsic permeability for continuum flow (K_D), [m^2] can be expressed according to Darcy's law:

$$K_D = \frac{\mu_g L_0 Q_t}{\Delta P A} = \frac{\pi}{128} \frac{6 - D_f}{D_f - D_\tau + 4} \left(\frac{(D_f - 4)\chi_{min}}{\ln \varphi}\right)^2 \left(\frac{\chi_{max}}{L_0}\right)^{8-D_\tau} \left[1 - \left({\chi_{min}}/{\chi_{max}}\right)^{D_f - D_\tau + 4}\right] \tag{14}$$

where $\chi_{max}^{10-D_\tau}/L_0^{8-D_\tau}$ is transformed to $\xi(\chi_{max}/L_0)^{8-D_\tau}$ to allow both χ_{max} and L_0 to follow the same fractal behaviour. According to Yu and Li (2001), $\xi = \chi_{max}^2 = \left((D_f - 4)\chi_{min}/\ln \varphi\right)^2$. Note that χ_{min} and χ_{max} are pore size limits of the continuum flow regime.

Moreover, the fractal model to predict apparent gas permeability is based on the gas slip flow rate through a single tortuous capillary q_g that can be obtained by correlating the viscous Poiseuille flow (q_L) and the Knudsen number ranging between $0.001 < K_n < 0.1$:

$$q_g = f(K_n)\, q_L \tag{15}$$

where $f(K_n)$ is the correlation coefficient (Wang et al., 2019), which can be expressed as (Freeman et al., 2011):

$$f(K_n) = 1 + 4K_n = 1 + \frac{4\delta}{\chi} \tag{16}$$

Here, δ is the mean free path [m] from kinetic theory:

$$\delta = \frac{\mu_g}{\bar{p}}\sqrt{\frac{\pi RT}{2M}} \tag{17}$$

where $\bar{p}$ is the mean gas pressure [Pa]; R represents the universal gas constant [J/(mol K)]; T is the temperature [K], and M is the gas molecular weight [g/mol]. The total gas flow rate for tortuous capillaries can be expressed as:

$$Q_t = -\int_{\chi_{min}}^{\chi_{max}} q_g(\chi)dN(\chi) \tag{18}$$

Substituting Equations (2), (4), (11), (15), and (16) into Equation (18), results in:

$$\begin{aligned} Q_t = \frac{\pi\Delta P}{128\mu_g}\frac{6-D_f}{D_f-D_\tau+4}\frac{\chi_{max}^{10-D_\tau}}{L_0^{7-D_\tau}}\left[1-\left({\chi_{min}}/{\chi_{max}}\right)^{D_f-D_\tau+4}\right]\Bigg\{1 \\ + \frac{4\mu_g}{\chi_{max}\bar{p}}\frac{\left(D_f-D_\tau+4\right)\left(1-\left({\chi_{min}}/{\chi_{max}}\right)^{D_f-D_\tau+3}\right)}{\left(D_f-D_\tau+3\right)\left(1-\left({\chi_{min}}/{\chi_{max}}\right)^{D_f-D_\tau+4}\right)}\sqrt{\frac{\pi RT}{2M}}\Bigg\} \end{aligned} \tag{19}$$

By combining Darcy's law and Equation (19), the apparent permeability (K_{app}), is:

$$K_{app} = \frac{\mu_g L_0 Q_t}{\Delta P A} = K_L + \frac{b}{\bar{p}} \tag{20}$$

where the intrinsic permeability (K_L) is equivalent to:

$$\begin{aligned} K_L = \frac{\pi}{128}\frac{6-D_f}{D_f-D_\tau+4}\left(\frac{\left(D_f-4\right)\chi_{min}}{\ln\varphi}\right)^2\left(\frac{\chi_{max}}{L_0}\right)^{8-D_\tau}\Big[1 \\ -\left({\chi_{min}}/{\chi_{max}}\right)^{D_f-D_\tau+4}\Big] \end{aligned} \tag{21}$$

and the slip factor (b) [Pa]:

$$b = \frac{4\mu_g}{\chi_{max}} \frac{\left(D_f - D_\tau + 4\right)\left(1 - \left({}^{\chi_{min}}/_{\chi_{max}}\right)^{D_f - D_\tau + 3}\right)}{\left(D_f - D_\tau + 3\right)\left(1 - \left({}^{\chi_{min}}/_{\chi_{max}}\right)^{D_f - D_\tau + 4}\right)} \sqrt{\frac{\pi RT}{2M}} \quad (22)$$

Note that χ_{min} and χ_{max} are the pore size limits of the slip flow regime, mainly depending on pressure and temperature. The total intrinsic permeability of the entire pore size range can be calculated by combining the intrinsic permeabilities associated with continuum flow and slip flow regimes; $K_t = K_D + K_L$. K_D and K_L have similar expressions, but they are not necessarily equal since these are intrinsic for different pore size ranges. The fractal permeability models are valid for SANS-derived fractal dimensions (D_f and D_τ), only.

3.2 Diffusion Fractal Model

Information on diffusional flux or effective diffusion coefficients (D_{eff}) are crucial to analyse the dissipation of gases in the interconnected pore structure of mudrocks (Amann-Hildenbrand et al., 2012; Busch et al., 2018). Fractal dimensions obtained from SANS data can be utilised to develop a fractal model for the estimation of diffusive transport, D_{eff} (Busch et al., 2018). The fractal model is based on Fick's law (Fick, 1855), and relates the diffusive flux to the gradient of the concentration along the diffusing path. The gas flow rate through a single tortuous capillary, $q_J(\chi)$, is given by Fick's law (Zheng et al., 2018):

$$q_J(\chi) = D_c A(\chi) \frac{\Delta C}{L(\chi)} \quad (23)$$

where $A(\chi) = \frac{\pi}{4}\chi^2$ is the pore area, ΔC is the concentration difference, and $L(\chi)$ is the tortuous length of a capillary tube that is obtained by Equation (4). D_c is the gas diffusion coefficient in the porous material, which is expressed as (Ghanbarian et al., 2013):

$$D_c = D_b \bar{\tau}^{-\alpha} \quad (24)$$

where D_b is the diffusion coefficient of diffusing species in bulk fluid (typically water or brine) and $\bar{\tau}$ is average tortuosity. α varies between $1 \leq \alpha \leq 2$, while 1 indicates smooth and 2 rough pores (Moldrup et al., 2001; Zheng et al., 2018). For a smooth pore system, $\bar{\tau}^{-1}$ is termed the pore continuity (Moldrup et al., 2001). Using the Wheatcraft and Tyler (1988) modification, gas diffusion coefficient in a tortuous capillary is thus obtained by:

$$D_c = D_b \bar{\tau}^{D_f-1} \tag{25}$$

where D_f is the fractal dimension.

The total gas flux for diffusion through a tortuous bundle of capillaries with the total cross section area A can be expressed as:

$$Q_J = -\int_{\chi_{min}}^{\chi_{max}} q_J(\chi) dN(\chi) \tag{26}$$

Substituting Equations (2), (4), (23), and (25) into Equation (26), results in:

$$Q_J = \frac{\pi}{4} D_b \bar{\tau}^{D_f-1} \Delta C \frac{6-D_f}{D_f-D_\tau+2} \frac{\chi_{max}^{8-D_\tau}}{L_0^{7-D_\tau}} \left(1 - \left(\frac{\chi_{min}}{\chi_{max}}\right)^{D_f-D_\tau+2}\right) \tag{27}$$

The diffusive gas flux across A can be obtained by Fick's law (Crank, 1975):

$$Q_J = D_{eff} A \frac{\Delta C}{L_0} \tag{28}$$

where $A = L_0^2$. By combining Equations (27) and (28), the effective diffusion coefficient (D_{eff}) based on the fractal model is:

$$D_{eff} = \frac{\pi}{4} D_b \bar{\tau}^{D_f-1} \frac{6-D_f}{D_f-D_\tau+2} \left(\frac{\chi_{max}}{L_0}\right)^{8-D_\tau} \left(1 - \left(\frac{\chi_{min}}{\chi_{max}}\right)^{D_f-D_\tau+2}\right) \tag{29}$$

Equation (29) represents the effective diffusion coefficient as a function of the diffusion coefficient of diffusing species in bulk fluid (D_b), fractal dimensions (D_f and D_τ), and structural parameters including tortuosity ($\bar{\tau}$), minimum (χ_{min}) and maximum (χ_{max}) pore sizes, and a straight capillary tube (L_0) with τ=1. D_τ is calculated using Equation (6), $\bar{\tau}$ from Equation (7), and L_0 from Equation (10). If $K_n \ll 1$, the molecular diffusion transport mode is advection-diffusion in which $D_{eff} = D_0 \equiv \delta\bar{v}/3$ where D_0 is the coefficient of molecular diffusion defined by the kinetic theory of gases and $\bar{v}$ is the mean molecular velocity [m/s]. If Knudsen diffusion is characterised by $K_n \gg 1$, $D_{eff} = D_{Kn} \equiv \bar{\chi}\bar{v}/3$ where D_{Kn} is the Knudsen diffusion coefficient. In the intermediate regime, $D_{eff} = D_{im} = ({D_0}^{-1} + {D_{Kn}}^{-1})^{-1}$, where D_{im} is the intermediate diffusion coefficient (Tartakovsky and Dentz, 2019). Depending on PSD and K_n, D_{eff} can be one

or a combination of these diffusion coefficients. The fractal diffusion model is valid for SANS-derived fractal dimensions (D_f and D_τ), only.

4 Results

4.1 Application of Knudsen Number (K_n) to Transport Phenomena

We used K_n to characterise fluid flow regimes in mudrocks. For an ideal gas and an inverse power law collision model, the Knudsen number is defined as $K_n = \delta/\chi$, where δ is the mean free path (MFP) of a gas molecule and χ is the pore size. MFP is obtained by (Colin, 2014):

$$\delta = \frac{\kappa \mu_g \sqrt{\frac{RT}{M}}}{P} \tag{30}$$

where $\mu_g$is gas viscosity [Pa.s], R = 8.315 J/mol.K being the universal gas constant, T is temperature [K], M is molecular weight [Kg/mol], and P is pressure [Pa]. κ represents intermolecular collisions between gas molecules confined in the pore system. Koura and Matsumoto (1991); (1992) introduced the variable soft sphere (VSS) model, which corrects the MFP and the collision rate by expressing the deflection angle taken by the molecule after a collision. Accordingly, the intermolecular collision coefficient κ is obtained by:

$$\kappa = \frac{4\zeta(7-2\eta)(5-2\eta)}{5(\zeta+1)(\zeta+2)\sqrt{2\pi}} \tag{31}$$

in which ζ is the exponent for the VSS model and η is the temperature exponent of the coefficient of viscosity (viscosity index) for a given gas. These exponents are available in Bird (1994) for a range of gases (e.g., H_2, CO_2, or CH_4).

Table 2 summarises the pore size boundaries of different fluid flow regimes, and Figure 1 presents the Knudsen number as a function of depth (pore pressure and temperature) for different pore sizes ranging from macropores to meso- and micropores. The Knudsen number decreases with depth for a given pore size, and it becomes progressively smaller towards larger pores at constant P-T conditions. Accordingly, at shallow present-day burial depth, organic lean mudrocks are dominated by transitional flow in micro- and smaller mesopores, followed by slip and continuum flow in larger meso- and macropores. Organic rich mudrocks at deeper present-

day burial depth accommodate slip flow and continuum flow within small and large pores, respectively. Furthermore, Knudsen numbers calculated for the mean pore size of all mudrocks ($\overline{Kn}$) show that slip flow is the dominant transport mechanism. This slip flow is taking place in the mesopore range, which has the highest population of pores (Figure 1).

Table 2. Pore size boundaries of the fluid flow regime. Note that only one sample is presented for each mudrock but may not represent the entire sample set for that mudrock.

Sample Set	**Sample ID**	D_{pd}	T	$\bar{P}_p$	**Gas**	**Phase**	δ	**Pore Size Boundaries**			
		m	K	MPa			nm	nm			
							Kn:	0.001	0.1	10	100
							Flow:	continuum	slip	transition	free molecular
Organic Lean Mudrocks											
Opalinus Clay	CCP01	250	291	2.5	H_2	sc	3.09	3095	31.0	0.31	0.031
Boom Clay	K2	233	290	2.3	H_2	sc	3.31	3312	33.1	0.33	0.033
Våle Shale	VS01	2500	319	11.8	CO_2	sc	0.69	687	6.9	0.07	0.007
Carmel Claystone	NPS083	200	289	2.0	CO_2	gas	1.07	1074	10.7	0.11	0.011
Big Hole Carmel	BH2-CC16b	200	289	2.0	CO_2	gas	1.07	1074	10.7	0.11	0.011
Entrada Siltstone	EPS-3071	222	290	2.2	CO_2	gas	0.96	957	9.57	0.10	0.010
Organic Rich Mudrocks											
Posidonia Shale	RWEP14	2500	358	24.6	CH_4	sc	0.23	233	2.3	0.02	0.002
Carboniferous Shale	KB186-15	1187	319	11.7	CH_4	sc	0.46	464	4.6	0.05	0.005
Bossier Shale	SCN3-6	3746	395	36.8	CH_4	sc	0.19	192	1.9	0.02	0.002
Haynesville Shale	HSA03	4200	409	41.2	CH_4	sc	0.18	179	1.8	0.02	0.002
Eagle Ford Shale	ESF01	3700	394	36.3	CH_4	sc	0.20	199	2.0	0.02	0.002
Jordan Shale	JS04	1750	335.5	17.19	CH_4	sc	0.37	365.46	3.65	0.04	0.004
Newark Shale	NS01	3962	402	38.9	CH_4	sc	0.19	187	1.9	0.02	0.002

D_{pd}: present-day burial depth; T: temperature; $\bar{P}_p$: intrinsic pore fluid pressure; sc: supercritical. Intrinsic pore fluid pressure is expressed as $\bar{P}_p = \rho_p g\, D_{pd}$; $\bar{P}_p$ is defined as the pressure averaged over the pore area of a representative elementary area (REA) where ρ_p is the density of the pore fluid (water, 1000 Kg/m^3) and g is the acceleration due to gravity (Zhao et al., 1998). It should be noted that Jordan shale is an oil-bearing formation, however, CH_4 is considered since Knudsen number is representative for gas systems only. Full results are listed in the Supporting Information (S3.1).

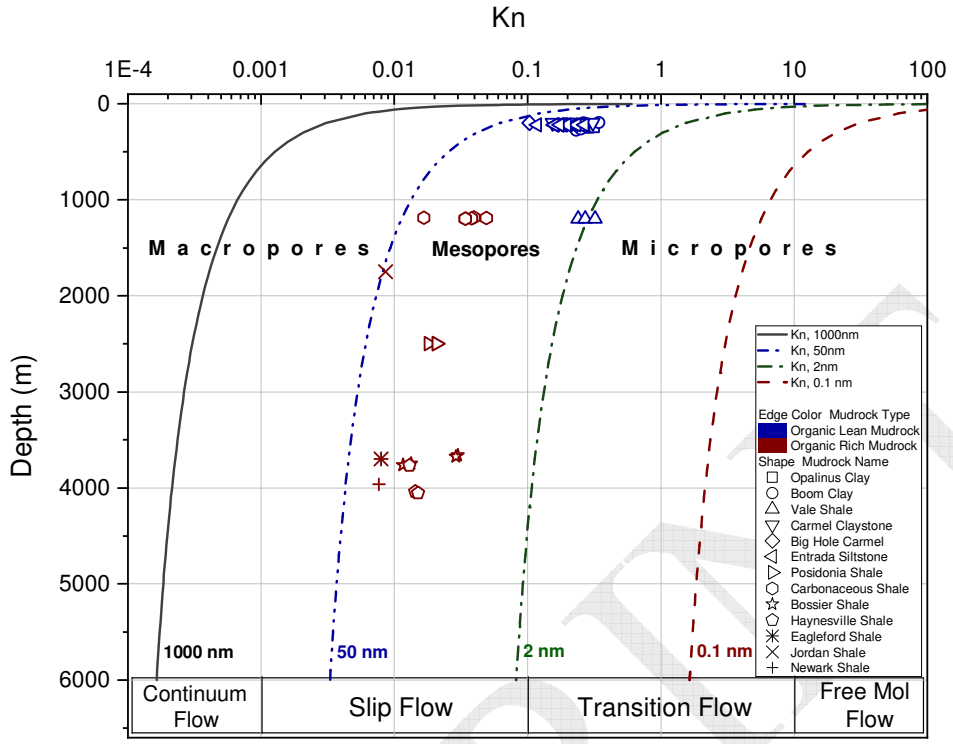

Figure 1. K_n versus depth. Open symbols represent $\overline{Kn}$ of samples considering MFP of guest fluid (H_2, CO_2, CH_4) at current depth and average pore size. Mol: molecular.

4.2 Darcy/Apparent Permeability and Effective Diffusion Coefficient (K_D, K_{app}, and D_{eff})

Pore characteristics of the individual samples are necessary to obtain K_D, K_{app}, and D_{eff}. These include fractal dimensions (D_f), tortuosity fractal dimension (D_τ), pore volumes, porosities, average (mean) pore size, as well as minimum and maximum pore sizes (see Supporting Information S3.2). Table 3 summarises calculated mudrock permeabilities and diffusivities using the fractal models and compares them with experimental values on twin sample plugs obtained from published data. The results consistently show higher plug compared to fractal permeabilities (by about 0.25-1.0 order of magnitude). The Darcy fractal permeabilities appear significantly lower than apparent fractal permeability in Opalinus, Boom, and Våle Shale whereas the difference between K_D and K_{app} is less significant in Carmel, Big Hole, Entrada, and most of the organic rich mudrocks. D_τ values are divided into two separate ranges (organic lean or organic rich mudrocks). In both separate ranges, K_D and K_{app} permeabilities increase with increasing D_τ. This finding is invalid when considering all mudrocks. Furthermore, K_D is

positively correlated to D_f in organic lean mudrocks, only. K_{app} shows a weak positive correlation with D_f for all mudrocks.

The fractal diffusion coefficients are in accordance with experimentally determined D_{eff} values, although the relative deviations of fractal D_{eff} values from experimental findings vary between 0.01-0.7 order of magnitude for Opalinus Clay samples using tritiated water (HTO) and between 0.01-0.93 order of magnitude for Boom Clay samples using HTO and CH_4. Experimental findings for Boom Clay vary only slightly (Busch et al., 2018), suggesting that the pore structure is rather uniform between samples. Similarly, the diffusion fractal model suggests that Boom Clay samples are composed of a uniform pore structure as D_f values differ slightly with values ~ 2.9. The wide range of fractal dimensions (2.0-3.0) obtained by SANS gives good confidence in the approach of using fractal dimensions obtained by SANS. This allows capturing the heterogeneity of the pore structures, which increases with an increase in fractal dimension. A detailed discussion of SANS based fractal model to understand diffusive transport parameter has been provided previously by Busch et al. (2018). The authors showed that model findings match experimental results well and SANS data provide a reliable method to retrieve effective diffusion coefficients. The technique enables measurements at different scales and orientations, thus allowing to understand the relationship of transport properties (porosity, SSA, and PSD apart from D_{eff}) to other rock properties, such as mineralogy.

Table 3. Summary of permeabilities and effective diffusion coefficients of representative mudrock samples using the fractal models and experiments on plug samples.

Sample Set	Sample ID	$D_{f,Darcy}$	$D_{\tau,Darcy}$	$L_{0,Darcy}$*	φ_{Darcy}	K_{Darcy}
		-	-	μm	-	m^2
Opalinus Clay	CCP01	2.67	1.81	72.862	0.009	5.11E-22
Boom Clay	K2	2.83	1.88	61.385	0.014	1.29E-21
Våle Shale	VS01	2.76	1.86	63.246	0.013	1.35E-21
Carmel Claystone	NPS083	1.83	1.60	159.484	0.001	3.75E-24
Big Hole Carmel	BH2-CC16b	1.64	1.60	145.452	0.002	9.22E-24
Entrada Siltstone	EPS-3071	1.61	1.63	123.342	0.002	4.03E-23
Posidonia Shale	RWEP14	2.77	2.32	65.499	0.012	3.88E-23
Carboniferous Shale	KB186-15	2.79	2.26	87.711	0.007	4.52E-24
Bossier Shale	SCN3-6	2.81	2.26	86.389	0.007	4.93E-24
Haynesville Shale	HSA03	2.96	2.37	57.464	0.017	5.38E-23
Eagle Ford Shale	ESF01	2.60	2.28	73.614	0.009	2.17E-23

Jordan Shale	JS04	2.79	2.34	60.204	0.014	6.82E-23
Newark Shale	NS01	2.87	2.25	94.844	0.006	2.26E-24

Table 3. (continued).

Sample Set	$D_{f,slip}$	$D_{\tau,slip}$	$L_{0,slip}$*	φ_{slip}	$K_{apparent}$	K_{total}	$K_{experimental}$	**Relative Error**
	-	-	μm	-	m^2	m^2	m^2	$\lvert(K_{exp}-K_t)/K_{exp}\rvert$
Opalinus Clay	2.93	2.73	10.143	0.121	1.82E-21	2.29E-21	5.90E-21	0.61
Boom Clay	2.99	2.76	8.965	0.154	4.06E-21	5.51E-21	1.00E-20	0.45
Våle Shale	2.95	2.77	8.789	0.156	4.94E-21	6.28E-21	--	--
Carmel Claystone	2.89	2.54	23.886	0.024	4.31E-24	8.01E-24	--	--
Big Hole Carmel	2.86	2.57	19.831	0.033	1.62E-23	2.54E-23	--	--
Entrada Siltstone	2.93	2.60	17.897	0.042	3.31E-23	6.34E-23	--	--
Posidonia Shale	2.48	2.36	1.516	0.047	1.26E-22	1.63E-22	1.00E-22	0.62
Carboniferous Shale	2.51	2.26	2.006	0.028	1.46E-23	1.87E-23	--	--
Bossier Shale	2.66	2.25	2.202	0.025	5.67E-24	1.05E-23	--	--
Haynesville Shale	2.86	2.40	1.574	0.052	5.46E-23	1.26E-22	--	--
Eagle Ford Shale	2.50	2.26	1.760	0.036	3.52E-23	5.63E-23	--	--
Jordan Shale	2.63	2.35	1.406	0.058	2.71E-22	2.28E-22	--	--
Newark Shale	2.57	2.23	2.470	0.019	2.89E-24	5.11E-24	3.00E-23	0.88

Table 3. (continued).

Sample Set	***Solute***	D_b	φ	D_f	L_0*	τ	D_τ	$D_{experimental}$	D_{eff}	**Relative Error**
		m^2/sec	-	-	μm	-	-	m^2/sec	m^2/sec	$\lvert(D_{exp}-D_{eff})/D_{exp}\rvert$
Opalinus Clay	HTO	1.60E-09	0.240	2.94	13.394	2.49	2.87	5.4E-11	6.98E-11	0.29
Boom Clay	HTO	1.60E-09	0.360	2.99	10.212	1.82	2.91	1.8E-10	1.57E-10	0.13
Våle Shale	CO_2	1.70E-09	0.385	2.96	9.574	1.73	2.92	--	2.16E-10	--
Carmel Claystone	CO_2	1.70E-09	0.026	2.85	45.094	19.81	2.67	--	3.89E-12	--
Big Hole Carmel	CO_2	1.70E-09	0.046	2.73	32.220	11.16	2.70	--	7.16E-12	--
Entrada Siltstone	CO_2	1.70E-09	0.071	2.79	26.053	7.41	2.75	--	1.30E-11	--
Posidonia Shale	CH_4	1.80E-09	0.065	2.77	27.208	8.06	2.73	--	1.20E-11	--
Carboniferous Shale	CH_4	1.80E-09	0.041	2.79	35.090	12.67	2.68	--	6.36E-12	--
Bossier Shale	CH_4	1.80E-09	0.049	2.81	31.838	10.52	2.69	--	8.15E-12	--
Haynesville Shale	CH_4	1.80E-09	0.083	2.96	25.158	6.40	2.77	--	1.58E-11	--
Eagle Ford Shale	CH_4	1.80E-09	0.054	2.60	29.032	9.72	2.68	--	8.22E-12	--
Jordan Shale	CH_4	1.80E-09	0.103	2.79	17.177	5.58	2.33	--	9.48E-12	--
Newark Shale	CH_4	1.80E-09	0.033	2.87	39.818	15.44	2.67	--	5.32E-12	--

* By definition, L_0 is smaller than the sample thickness. Porosity values are obtained from SANS measurements. Experimental data are not obtained from the same samples, but twin samples. Studies reporting experimental D_{eff} of the twin samples are unavailable. The experimental permeability of Opalinus Clay is taken from Amann-Hildenbrand et al. (2015), Posidonia Shale

after Ghanizadeh et al. (2014b), and Newark Shale after Fink et al. (2018). The experimental permeabilities are corrected for Klinkenberg effect as well as for unstressed condition. Experimental D_{eff} of Boom Clay samples have been taken from Jacops et al. (2017) and Opalinus Clay samples from Pearson et al. (2003). We assume different solutes diffusing in the aqueous phase. D_b of different solutes were calculated from the model developed by Boudreau (1997). Full results are listed in Supporting Information (S3.3).

5 Discussion

5.1 Dominant Flow Regimes in Mudrocks

Organic lean mudrocks that are currently at shallow burial depths of < 300 m (Opalinus, Boom, Carmel, and Entrada), correspond to low hydrostatic pore pressures of 2-3 MPa, low temperatures of 287-292 K and large mean free path length of 2.4-5.2 nm. This results in transitional flow within pores less than ~ 30 nm, continuum flow within pores larger than ~ 3 µm, and slip flow within pores between 30 nm and 3 µm (Figure 2-A). Figure 2-A suggests an increasing control of slip flow in meso- and macropores, with a contribution of > 50 % of the relative pore volume (Figure 2-B). Within these rocks, transitional flow determines the flow regime in micropores and in a large fraction of the mesopores and contributes to ~ 20-40 % of the relative pore volume.

Organic rich mudrocks (gas shales) are subject to greater present-day burial depth of > 1000 m, corresponding to higher pore pressures of 12-40 MPa (assuming hydrostatic conditions) and temperatures of 320-420 K, and lower mean free path lengths of 0.15-0.3 nm. This results in transition flow in micropores (< 2 nm), slip flow in meso- and smaller macropores (~ 2-250 nm), and continuum flow in larger macropores (> 250 nm) (Figure 2-C). Figure 2-C suggests that organic rich mudrocks are rather dominated by slip/continuum flow. Lower pore pressures for Posidonia and Carboniferous have caused slip flow to become more dominant and higher pore pressure resulted in continuum flow dominating > 50 % of the relative pore volume in Bossier, Haynesville, Eagle Ford, and Newark Shales (Figure 2-D). Therefore, continuum flow will become increasingly important in smaller pores as the pore pressure increases and slip flow will become increasingly dominant for larger pores during pore pressure decrease which becomes relevant when depleting shale gas reservoirs. Although porosity in mudrocks can be high with

values well above 10 %, a large fraction of this porosity can be associated with pore sizes where molecule/surface interactions dominate and only diffusion or gas slippage is possible. In addition, pore orientation for high porosity mudrocks might be anisotropic due to the increased clay content, improving horizontal yet limiting vertical flux rates (Dabat et al., 2020). The high specific surface area associated with clay minerals and kerogen allows gases (CO_2, CH_4 or H_2) to form a sorptive layer on the pore surfaces (Rother et al., 2007; Rother et al., 2014), changing pore throat or pore body sizes. This results in an effective porosity reduction, thus a possible change in pore connectivity during production and/or storage. Therefore, average pore sizes and related distributions are the result of random aspect ratios (pore body/pore throat) over the entire pore size range (Busch et al., 2017). These are important controls on fluid flow, diffusion, and sorption mechanisms in mudrocks (Rezaeyan et al., 2019a; 2019b; 2019c; Seemann et al., 2019).

For the samples studied here, the MFP is close to the average pore size in organic lean but smaller than that in organic rich mudrocks. As a result, transition flow occupying the micropore domain becomes more important, leading to a higher probability of intermolecular collisions that requires a molecular approach to solve the fluid flow in direct simulation Monte-Carlo and/or Lattice-Boltzmann models (Agarwal et al., 2001). In transition flow, the continuum approach and thermodynamic equilibrium assumptions of the Navier-Stokes equations are no longer valid (Barber and Emerson, 2006). The slip boundary condition does not apply due to negligible collisions between molecules and the pore wall (Li et al., 2011); however, the slip flow model may still partly be used in the transition regime particularly for the organic lean mudrocks with average pore sizes of ~ 30 nm. In slip flow, the thickness of the Knudsen layer that forms in the vicinity of the mudrock pore wall approaches the MFP in the meso- and macropores. This results in gas not being in thermodynamic equilibrium, leading to gas slippage in the interconnected pore structure (Dongari et al., 2011; Zhang et al., 2006). The Navier-Stokes equations remain applicable, provided the boundary conditions are modified in the expression of a velocity slip as well as a temperature jump at the wall of slip domain pore sizes (Colin, 2011). In continuum flow, fluid flow is the continuity of temperature and velocity between the fluid and the pore wall in the macropores of mudrocks. Flow is solved by the compressible Navier-Stokes equations, the ideal gas equation of state (thermodynamic equilibrium), and classic boundary conditions in Lattice-Boltzmann models (Bird, 1994; Colin, 2014). According to above, we argue that transport phenomena in mudrocks are pore size dependent. This suggests that the

multi-aspect interaction between bulk volume flow, sorption and transport mechanisms must be adequately addressed in experimental and numerical investigations. By analysing the pore size distribution, total porosity, and specific surface area in relation to pore orientation, we can improve our understanding of transport phenomena and sorption relationships.

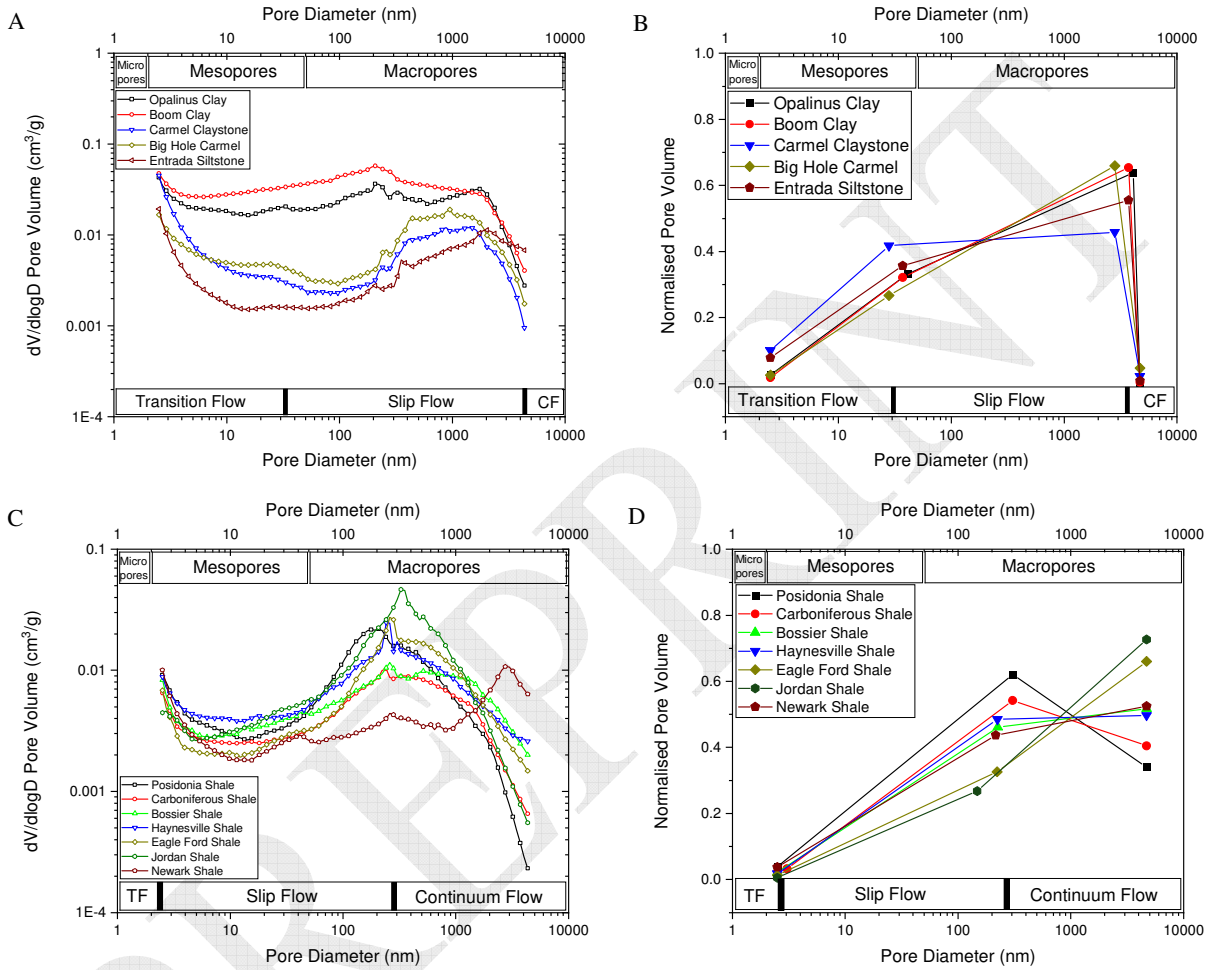

Figure 2. Pore size dependent transport phenomena related to dominant fluid flow regime: (A) pore size distribution and (B) relative pore volume of organic lean mudrocks; (C) pore size distribution and (D) relative pore volume of organic rich mudrocks. TF: transition flow and CF:

continuum flow. Pore volume distributions of all mudrocks is provided in Supporting Information (S3.4).

5.2 Transport Properties for Dominant Flow Regimes

Figure 3 illustrates Darcy permeability (K_D) for continuum flow and apparent permeability (K_{app}) and effective diffusion coefficients (D_{eff}) for diffusion flow in all mudrocks obtained by the fractal models. We find that the difference between K_{app} and K_D decreases with decreasing porosity, which can be related to mean pore sizes which decrease with an increase in present-day burial depth (Figure 3-A). Unlike, analytical or numerical models or laboratory tests, fractal models can define permeabilities for dominant flow regimes, which depend on pore size range, pressure, temperature, and molecular size. The permeability fractal models permit distinguishing between the two dominant fluid flow regimes, continuum and slip flow, if pore characteristics (e.g., φ, D_f, D_τ, etc.) are individually specified for each regime. As such, the incorporation of fractal features with pore size dependent transport phenomena seems useful to allow for an improved prediction of permeability in mudrocks.

Micro-fractures can be one of reasons for the difference between K_t and K_{exp}. Sample plugs contain both matrix and fractures while SANS-fractal data represent matrix properties only. Matrix permeabilities on gas shales have been determined experimentally by Fisher et al. (2017) and Fink et al. (2017a) based on the pressure pulse-decay method on crushed samples. The matrix permeability of crushed samples was overestimated from K_{exp} by up to 6 orders of magnitude. There are many reasons for the difference, e.g. errors in calculating permeability from pressure transients, suitability crushed rocks for permeability measurements Fisher et al. (2017). In comparison, the total fractal permeability (K_{total}) determined in this study varies by 0.1-1 order of magnitude from K_{exp}, only (Table 3). Our results suggest that the tortuosity fractals combined with fractal dimensions capture tortuous pore structure with slit like cross-sectional shapes in mudrocks, allowing for an improved estimate of permeability. Nevertheless, predictions based on fractal models match reasonably well with experimental data for samples having porosities $\varphi > 0.10$, while the match is insignificant for lower porosity samples ($\varphi < 0.10$). Similar findings have been reported by previous studies (Chen and Yao, 2017; Xiao et al., 2014; Zhang et al., 2018; Zheng et al., 2018). We suggest pore size limits be constrained to the

length in which fractal criteria are satisfied for the individual flow regime so both D_f and D_τ represent the heterogeneity of mudrocks.

Clay type/content and compaction (maximum stress) controls the porosity-permeability relationship in mudrocks. With increasing maximum burial depth, mechanical and chemical compaction result in a porosity reduction (Bjørlykke, 2006), leading to a decrease in permeability. In contrast, the abundance of framework grains (mainly quartz and carbonates) can help preserving macropores in the absence of chemical compaction, resulting in increased permeabilities. To exemplify this, we can focus on Entrada and Carmel samples, originating from the same location with depth differences of few tens of meters only. Entrada consists of ~ 60 wt. % quartz, dolomite, and feldspar and ~ 30 wt. % illite. Carmel consists of ~15% wt. quartz, dolomite, and feldspar with ~ 80 wt. % illite. As a result, the average pore size of Carmel is ~ 5 nm which is significantly lower than for Entrada (~ 7.8 nm), resulting in a significantly lower Darcy permeability due to micro-to-mesopores associated with the illite-rich matrix (Supporting Information, S2.1 and S3.1). Mudrocks however accommodate higher apparent than Darcy permeabilities resulting in a greater total permeability (K_t) since slip flow is commonly associated with macropores as well as part of the mesopores (~ 25 nm – 50 nm) (Supporting Information, S3.1). If a large fraction of macroporosity is interconnected throughout meso- to macropores, conductivity for flow increases in the pore network.

Furthermore, the permeability of mudrocks has been experimentally tested (Fink et al., 2017b; Gaus et al., 2019; Ghanizadeh et al., 2014a; Ghanizadeh et al., 2014b), clearly demonstrating that plug permeability and pore volume decreases with an increase in effective stress. In a uniform system, compaction is considered spatially constant, however, the compressibility of different minerals (e.g., clay versus quartz) can be quite different (Dautriat et al., 2011). Assuming that different pore sizes are associated with different mineralogy regardless of diagenetic history (e.g., clays with smaller, quartz/carbonate with larger pores), we can also speculate that the permeability dependence on stress varies over different pore sizes as well. While the permeability fractal model allows calculation of fluid pressure dependent gas permeability (Zhang et al., 2017), it cannot reproduce effective stress changes since all SANS measurements were done on unstressed samples. Of the samples tested in this study, we expect significant differences in mechanical properties (especially bulk moduli) and therefore

differences in stress relaxation of the pore space when bringing the samples to ambient conditions. This aspect cannot be addressed here and requires future work by potentially determining pore size distributions under applied stress. In contrast, stressed permeabilities conducted on sample plugs can only provide a bulk permeability assuming a certain flow regime that dominates. Constraining the fractal model to certain pore sizes provides pore size dependent (pressure-dependent) permeabilities that can be integrated with the dominant fluid flow mechanism.

Figure 3-B shows that the effective diffusion coefficient is positively correlated with porosity. Organic rich mudrocks are characterised by low effective diffusion coefficients with values on the order of ~ 1E-11 $m^2.s^{-1}$; high clay/kerogen content along with relatively higher present-day overburden stresses result in lower diffusion coefficients. For permeability, the pore throat diameter is the determining factor. In diffusion, tortuosity is a key control, which is again controlled by pore throat and pore body sizes that can change upon changes in effective stress and diagenesis (Fathi and Akkutlu, 2014). Yet, this does not invalidate the relationship of low permeability relating to low diffusivity and vice versa, as can be seen in Figure 3-C. Especially for high permeability and high diffusivity samples, a linear relation can be observed, indicating that pore throats are the key controls for both transport modes. We can assume that pore throat sizes are similar to the MFP and as such, concentration driven gas (e.g., CH_4, CO_2, H_2) diffusion is likely to control migration through these pores with pore throats (Amann-Hildenbrand et al., 2012; Gensterblum et al., 2015; Jarvie et al., 2007; Loucks et al., 2009; Ross and Bustin, 2008). Therefore, we can argue that the pressure-driven volume flow and molecular diffusion tend to become distinguishable in extremely low permeability rocks by segregating dominant flow regimes based on effective pore sizes.

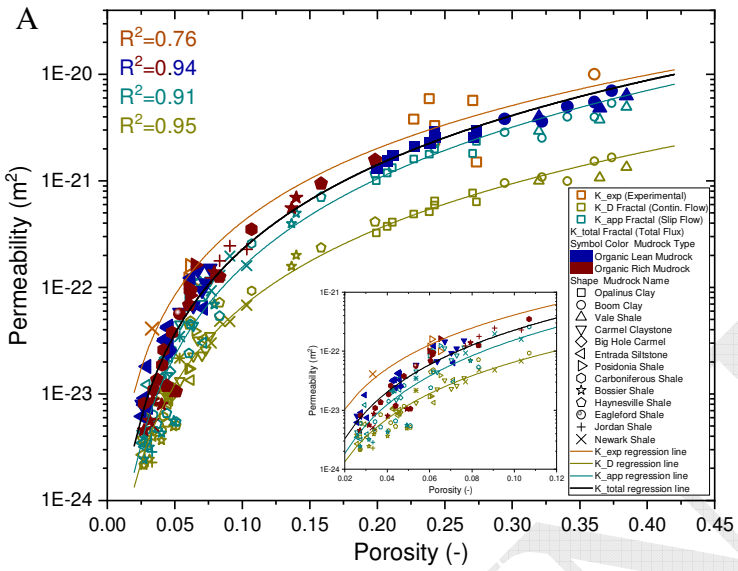
A
R2=0.76
R2=0.94
R2=0.91
R2=0.95
Permeability (m2)
1E-20
1E-21
1E-22
1E-23
1E-24
0.00
0.05
0.10
0.15
0.20
0.25
0.30
0.35
0.40
0.45
Porosity (-)
K_exp (Experimental)
K_D Fractal (Contin. Flow)
K_app Fractal (Slip Flow)
K_total Fractal (Total Flux)
Symbol Color Mudrock Type
Organic Lean Mudrock
Organic Rich Mudrock
Shape Mudrock Name
Opalinus Clay
Boom Clay
Vale Shale
Carmel Claystone
Big Hole Carmel
Entrada Siltstone
Posidonia Shale
Carboniferous Shale
Bossier Shale
Haynesville Shale
Eagleford Shale
Jordan Shale
Newark Shale
K_exp regression line
K_D regression line
K_app regression line
K_total regression line

1

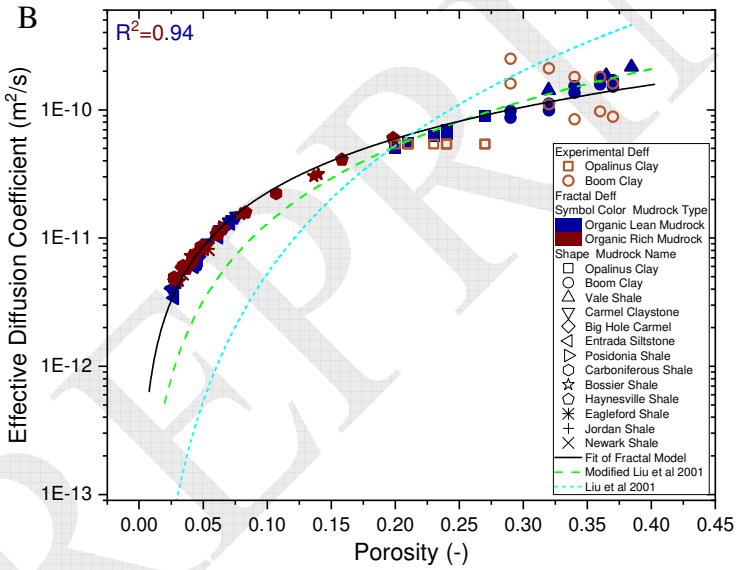
B
R2=0.94
Effective Diffusion Coefficient (m2/s)
1E-10
1E-11
1E-12
1E-13
0.00
0.05
0.10
0.15
0.20
0.25
0.30
0.35
0.40
0.45
Porosity (-)
Experimental Deff
Opalinus Clay
Boom Clay
Fractal Deff
Symbol Color Mudrock Type
Organic Lean Mudrock
Organic Rich Mudrock
Shape Mudrock Name
Opalinus Clay
Boom Clay
Vale Shale
Carmel Claystone
Big Hole Carmel
Entrada Siltstone
Posidonia Shale
Carboniferous Shale
Bossier Shale
Haynesville Shale
Eagleford Shale
Jordan Shale
Newark Shale
Fit of Fractal Model
Modified Liu et al 2001
Liu et al 2001

2

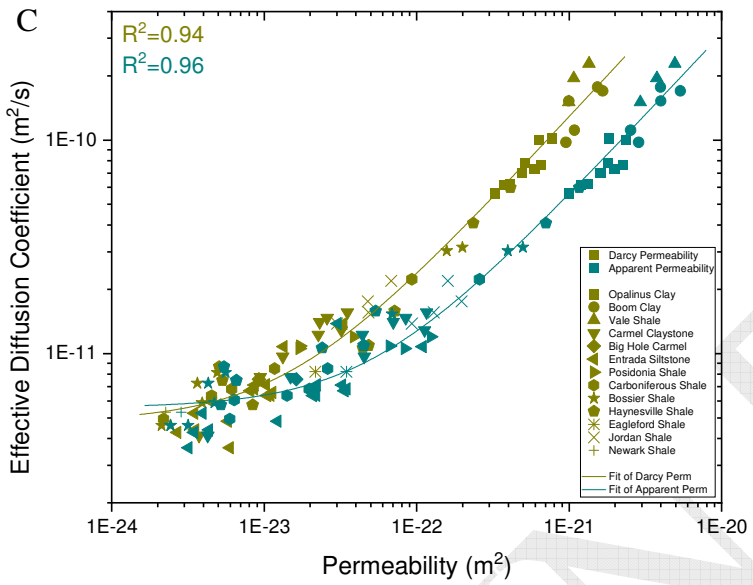

Figure 3. Pore size dependent transport properties using fractal models. (A) matrix permeabilities of the mudrocks calculated for continuum and slip flows (K_D and K_{app}, respectively) as well as plug permeabilities (K_{exp}), the insert plot shows permeabilities for individual samples with porosities ranging between 0.02 and 0.12; (B) effective diffusion coefficients (D_{eff}), the diffusion fractal model is compared with the Liu and Nie (2001) and modified Liu and Nie (2001) fractal model (Rezaeyan, 2021); (C) methane diffusion coefficient versus permeabilities (K_D and K_{app}). Non-linear curve fits are obtained using power functions.

6 Conclusions

Small angle neutron scattering resolves a wide range of mudrock pore sizes (2.5 nm – 5 µm). Fluid flow regimes in mudrocks vary depending on the pore sizes as well as pressure and temperature conditions. For some of the organic lean mudrocks studied, originating from low hydrostatic pore pressures (2-3 MPa) due to shallow depth, gas molecules develop transitional flow within micropores and mesopores with sizes up to 30 nm, slip flow in pore sizes between 30 nm – 3 µm, and continuum flow within pores > 3 µm. Most organic rich mudrocks studied originate from depth associated with high pore fluid pressures (12-40 MPa). Because of the smaller mean free path length at larger depths, continuum flow is dominant in macropores > ~ 250 nm, slip flow in smaller macropores and mesopores, and transitional flow in micropores. With a reduction in pressure during reservoir depletion in gas shale reservoirs, slip flow becomes more dominant for larger pore. In contrast, when injecting gases into the subsurface and pressure

is continuously increasing, continuum flow becomes increasingly dominant when gas is flowing through tight mudrocks. This shows that bulk volume flow related to pore pressure changes and pore size distributions needs to be addressed in experimental and numerical investigations. Further complexity relates to diffusion and sorption to understand bulk fluid migration in pore systems of mudrocks. By analysing the pore size distribution, total porosity and SSA in relation to pore orientation, we can inform fluid dynamic models to improve our understanding of these flow-diffusion-sorption relationships.

The study of gas transport in low permeability rocks revolves not only around the validity of dominant fluid flow regimes associated with different pore size ranges, but also their pore size dependent transport properties. Fractal models calculate Darcy permeability for continuum flow and apparent permeability and effective diffusion coefficients for slip/diffusional flow for the relevant pore sizes in mudrocks. Most mudrocks are characterised by higher apparent permeabilities than Darcy permeability, since slip flow dominates a wide pore size range of ~ 25 – 250 nm with large pore volumes of up to 70 %. If a large fraction of macroporosity is interconnected by meso- and macropores, this results in a higher conductivity to flow for the entire pore network. On the other hand, the increased nanoporosity with small pore throats results in high diffusivity. The pressure-driven volume flow and molecular diffusion tend to become distinguishable in low permeability rocks by segregating dominant flow regimes based on the effective pore sizes.

Nomenclatures

Alphabet Letters

A	m^2	Total cross area
A_p	m^2	Total pore area
b	Pa	Slip factor
D_f	-	Fractal dimension
D_b	m^2/s	Diffusion coefficient of diffusing species in bulk fluid
D_c	m^2/s	Gas diffusion coefficient
D_{pd}	m	Present-day burial depth
D_{eff}	m^2/s	Effective diffusion coefficients
D_{im}	m^2/s	Intermediate diffusion coefficients
D_{Kn}	m^2/s	Knudsen diffusion coefficients
D_0	m^2/s	Molecular diffusion coefficients
D_G	-	General topological dimension
D_τ	-	Tortuosity fractal dimension

$dV/dlogD$	cm^3/g	Logarithmic differential pore volume distribution
g	m/s^2	Gravitational acceleration
I; $I(Q)$	cm^{-1}	Scattering intensity
K_{app}	m^2	Apparent permeability
K_D	m^2	Darcy permeability
K_{exp}	m^2	Experimental permeability
K_L	m^2	Intrinsic permeability
K_t	m^2	Total matrix permeability
K_n	-	Knudsen number
$\overline{Kn}$	-	Average Knudsen number
L	nm	Tortuous length of capillary tubes
L_0	nm	Straight length of capillary tubes
M	g/mol	Atomic mass of the mixture; gas molecular weight
m	-	Slope; power-law exponent
N	-	Cumulative number of capillary tubes
N_A	mol^{-1}	Avogadro's number
P	Pa	Pressure
$\bar{P}_p$	Pa	Intrinsic pore fluid pressure
$\bar{p}$	Pa	Mean gas pore pressure
Q	$Å^{-1}$	Scattering vector
Q_J	$Kg.m^3/s$	Total gas diffusion flux
Q_t	m^3/s	Total gas flow rate
q_g	m^3/s	Gas slip flow rate
q_L	m^3/s	Gas Darcy flow rate
q_J	$Kg.m^3/s$	Diffusive gas flux
R	J/K/mol	Gas molecular constant
T	K	Temperature
VR_r	%	Vitrinite reflectance

Greek Letters

α	-	Tortuosity exponent
ΔC	Kg	Concentration difference
ΔP	Pa	Pressure gradient
δ	nm	Mean free path
ε	-	Ratio the straight length of capillary tubes to the average pore size
ζ	-	The exponent for the VSS model
η	-	Viscosity index
κ	-	Intermolecular collision coefficient for the VSS model
λ	Å	Wavelength
μ_g	Pa.s	Gas viscosity
$\bar{v}$	m/s	Mean molecular velocity
ξ	nm^2	Squared maximum pore size
ρ_p	g/cm^3	Pore fluid density
τ	-	Tortuosity
$\bar{\tau}$	-	Average tortuosity
φ	-	Porosity

χ	nm	Pore size or pore diameter
χ_{max}	nm	Maximum pore size
$\bar{\chi}; \chi_{mean}$	nm	Mean (average) pore size
χ_{min}	nm	Minimum pore size

Abbreviations

CF	Continuum Flow
HTO	Tritiated Water
IUPAC	International Union of Applied Chemistry
JCNS	Jülich Centre for Neutron Science
MATSAS	MATLAB for Small Angle Scattering
MFP	Mean Free Path
MLZ	Heinz Maier-Leibnitz Zentrum
PDSP	Polydisperse Spherical Model
PSD	Pore Size Distribution
SANS	Small Angle Neutron Scattering
sc	supercritical
SSA	Specific Surface Area
TF	Transition Flow
TOC	Total Organic Carbon
VSANS	Very Small Angle Neutron Scattering
VSS	Variable Soft Sphere

Acknowledgments

This work is based upon experiments performed at the KWS-1 and KWS-3 instruments operated by JCNS at the Heinz Maier-Leibnitz Zentrum (MLZ), Garching, Germany. We are very grateful for the possibility to conduct measurements at these instruments as well as to Artem Feoktystov for helping with the data collection. We are thankful to Pieter Bertier from Dynchem, Germany for useful discussions, and support in acquiring SANS data. We further thank Vito-Belgium, Elke Jacops, and Norbert Maes from SCK-CEN for providing Boom Clay samples, Swisstopo, Switzerland for providing Opalinus Shale samples, and Norske Shell, Norway for making Våle shale samples available to this study. Contributions to measurements and manuscript preparation by G.R. were supported by the Department of Energy, Office of Science, Office of Basic Energy Sciences, Chemical Sciences, Geosciences and Biosciences Division.

Supporting Information

The Supporting Information is available free of charge at https://doi.org/10.4121/14939133.

Additional text on the mudrock samples and experimental-analytical methods; more detailed descriptions of the results; 3 supplementary figures, and 7 supplementary tables.

References

Agarwal, R.K., Yun, K.-Y. and Balakrishnan, R., 2001. Beyond Navier–Stokes: Burnett equations for flows in the continuum–transition regime. Physics of Fluids, 13(10): 3061-3085.

Amann-Hildenbrand, A., Bertier, P., Busch, A. and Krooss, B.M., 2013. Experimental investigation of the sealing capacity of generic clay-rich caprocks. International Journal of Greenhouse Gas Control, 19: 620-641.

Amann-Hildenbrand, A., Ghanizadeh, A. and Krooss, B.M., 2012. Transport properties of unconventional gas systems. Marine and Petroleum Geology, 31(1): 90-99.

Amann-Hildenbrand, A., Krooss, B.M., Bertier, P. and Busch, A., 2015. Laboratory Testing Procedure for CO2 Capillary Entry Pressures on Caprocks. In: K.F. Gerdes (Editor), Carbon Dioxide Capture for Storage in Deep Geological Formations. CPL Press and BPCNAI.

Amireh, B.S., 1997. Sedimentology and palaeogeography of the regressive-transgressive Kurnub Group (Early Cretaceous) of Jordan. Sedimentary Geology, 112(1): 69-88.

Anovitz, L.M. and Cole, D.R., 2015. Characterization and Analysis of Porosity and Pore Structures. Reviews in Mineralogy and Geochemistry, 80(1): 61-164.

Bahadur, J., Melnichenko, Y.B., Mastalerz, M., Furmann, A. and Clarkson, C.R., 2014. Hierarchical Pore Morphology of Cretaceous Shale: A Small-Angle Neutron Scattering and Ultrasmall-Angle Neutron Scattering Study. Energy & Fuels, 28(10): 6336–6344.

Barber, R.W. and Emerson, D.R., 2006. Challenges in Modeling Gas-Phase Flow in Microchannels: From Slip to Transition. Heat Transfer Engineering, 27(4): 3-12.

Beckingham, L.E. and Winningham, L., 2020. Critical Knowledge Gaps for Understanding Water–Rock–Working Phase Interactions for Compressed Energy Storage in Porous Formations. ACS Sustainable Chemistry & Engineering, 8(1): 2-11.

Bird, G.A., 1994. Molecular Gas Dynamics and the Direct Simulation of Gas Flows. Clarendon Press.

Bjørlykke, K., 2006. Effects of compaction processes on stresses, faults, and fluid flow in sedimentary basins: Examples from the Norwegian margin, Geological Society Special Publication, pp. 359-379.

Blakey, R.C., Havholm, K.G. and Jones, L.S., 1996. Stratigraphic analysis of eolian interactions with marine and fluvial deposits, Middle Jurassic Page Sandstone and Carmel Formation, Colorado Plateau, U.S.A. Journal of Sedimentary Research, 66(2): 324-342.

Bossart, P. and Thury, M., 2008. Mont Terri Rock Laboratory Project, Programme 1996 to 2007 and Results, Wabern, Switzerland.

Boudreau, B.P., 1997. Diagenetic models and their implementation- Modelling transport and reactions in aquatic sediments. Berlin: Springer.

Bruggeman, C. and Craen, M.D., 2012. Boom Clay natural organic matter, Belgian Nuclear Research Centre, SCK•CEN, Mol, Belgium.

Bruns, B., Littke, R., Gasparik, M., van Wees, J.-D. and Nelskamp, S., 2016. Thermal evolution and shale gas potential estimation of the Wealden and Posidonia Shale in NW-Germany and the Netherlands: a 3D basin modelling study. Basin Research, 28(1): 2-33.

Busch, A. and Kampman, N., 2018. Fluid migration to surface from deep Geological CO2 Storage Sites. In: S. Vialle, J.W. Carey and J.B. Ajo-Franklin (Editors), AGU Monograph: Caprock Integrity in Geological Caprock Storage.

Busch, A., Kampman, N., Bertier, P., Pipich, V., Feoktystov, A., Rother, G., Harrington, J., Leu, L., Aertens, M. and Jacops, E., 2018. Predicting effective diffusion coefficients in mudrocks using a fractal model and small angle neutron scattering measurements. Water Resources Research, 54(9): 7076–7091.

Busch, A., Schweinar, K., Kampman, N., Coorn, A., Pipich, V., Feoktystov, A., Leu, L., Amann-Hildenbrand, A. and Bertier, P., 2016. Shale Porosity - What Can We Learn from Different Methods?, Fifth EAGE Shale Workshop, Catania, Italy.

Busch, A., Schweinar, K., Kampman, N., Coorn, A., Pipich, V., Feoktystov, A., Leu, L., Amann-Hildenbrand, A. and Bertier, P., 2017. Determining the porosity of mudrocks using methodological pluralism. Geological Society, London, Special Publications, 454.

Bustin, R.M., Bustin, A.M.M., Cui, X., Ross, D.J.K. and Pathi, V.S.M., 2008. Impact of shale properties on pore structure and storage characteristics, Society of Petroleum Engineers - Shale Gas Production Conference 2008, pp. 32-59.

Chalmers, G.R., Bustin, R.M. and Power, I.M., 2012. Characterization of gas shale pore systems by porosimetry, pycnometry, surface area, and field emission scanning electron microscopy/transmission electron microscopy image analyses: Examples from the Barnett, Woodford, Haynesville, Marcellus, and Doig units. American Association of Petroleum Geologists Bulletin, 96(6): 1099–1119.

Charlet, L., Alt-Epping, P., Wersin, P. and Gilbert, B., 2017. Diffusive transport and reaction in clay rocks: A storage (nuclear waste, CO2, H2), energy (shale gas) and water quality issue. Advances in Water Resources, 106: 39-59.

Chen, X. and Yao, G., 2017. An improved model for permeability estimation in low permeable porous media based on fractal geometry and modified Hagen-Poiseuille flow. Fuel, 210: 748-757.

Colin, S., 2011. Gas Microflows in the Slip Flow Regime: A Critical Review on Convective Heat Transfer. Journal of Heat Transfer, 134(2).

Colin, S., 2014. Chapter 2 - Single-Phase Gas Flow in Microchannels. In: S.G. Kandlikar, S. Garimella, D. Li, S. Colin and M.R. King (Editors), Heat Transfer and Fluid Flow in Minichannels and Microchannels (Second Edition). Butterworth-Heinemann, Oxford, pp. 11-102.

Crank, J., 1975. The Mathematics of Diffusion. Clarendon Press.

Cui, X., Bustin, A.M.M. and Bustin, R.M., 2009. Measurements of gas permeability and diffusivity of tight reservoir rocks: different approaches and their applications. Geofluids, 9(3): 208-223.

Curtis, M.E., Ambrose, R.J. and Sondergeld, C.H., 2010. Structural Characterization of Gas Shales on the Micro- and Nano-Scales, Canadian Unconventional Resources and International Petroleum Conference. Society of Petroleum Engineers, Calgary, Alberta, Canada.

Cussler, E.L., 1997. Diffusion: Mass transfer in fluid systems Cambridge University Press, Cambridge, UK, 525 pp.

Dabat, T., Porion, P., Hubert, F., Paineau, E., Dazas, B., Grégoire, B., Tertre, E., Delville, A. and Ferrage, E., 2020. Influence of preferred orientation of clay particles on the diffusion of water in kaolinite porous media at constant porosity. Applied Clay Science, 184: 105354.

Dautriat, J., Gland, N., Dimanov, A. and Raphanel, J., 2011. Hydromechanical behavior of heterogeneous carbonate rock under proportional triaxial loadings. Journal of Geophysical Research: Solid Earth, 116(B1).

Dawson, W.C. and Almon, W.R., 2010. Eagle Ford Shale variability: Sedimentologic influences on source and reservoir character in an unconventional resource unit. Gulf Coast Assoc. Geol. Soc., Trans., 60: 181-190.

Day-Stirrat, R.J., Schleicher, A.M., Schneider, J., Flemings, P.B., Germaine, J.T. and van der Pluijm, B.A., 2011. Preferred orientation of phyllosilicates: Effects of composition and stress on resedimented mudstone microfabrics. Journal of Structural Geology, 33(9): 1347-1358.

Dongari, N., Zhang, Y. and Reese, J.M., 2011. Modeling of Knudsen Layer Effects in Micro/Nanoscale Gas Flows. Journal of Fluids Engineering, 133(7).

Fathi, E. and Akkutlu, I.Y., 2014. Multi-component gas transport and adsorption effects during CO<inf>2</inf> injection and enhanced shale gas recovery. International Journal of Coal Geology, 123: 52-61.

Feoktystov, A.V., Frielinghaus, H., Di, Z., Jaksch, S., Pipich, V., Appavou, M.-S., Babcock, E., Hanslik, R., Engels, R., Kemmerling, G., Kleines, H., Ioffe, A., Richter, D. and Bruckel, T., 2015. KWS-1 high-resolution small-angle neutron scattering instrument at JCNS: current state. Journal of Applied Crystallography, 48(1): 61-70.

Fick, A., 1855. Ueber Diffusion. Annalen der Physik, 170(1): 59-86.

Fink, R., Amann-Hildenbrand, A., Bertier, P. and Littke, R., 2018. Pore structure, gas storage and matrix transport characteristics of lacustrine Newark shale. Marine and Petroleum Geology, 97: 525-539.

Fink, R., Krooss, B.M. and Amann-Hildenbrand, A., 2017a. Stress-dependence of porosity and permeability of the Upper Jurassic Bossier shale: an experimental study. Geological Society, London, Special Publications, 454.

Fink, R., Krooss, B.M., Gensterblum, Y. and Amann-Hildenbrand, A., 2017b. Apparent permeability of gas shales – Superposition of fluid-dynamic and poro-elastic effects. Fuel, 199: 532-550.

Fisher, Q., Lorinczi, P., Grattoni, C., Rybalcenko, K., Crook, A.J., Allshorn, S., Burns, A.D. and Shafagh, I., 2017. Laboratory characterization of the porosity and permeability of gas shales using the crushed shale method: Insights from experiments and numerical modelling. Marine and Petroleum Geology, 86: 95-110.

Freeman, C.M., Moridis, G.J. and Blasingame, T.A., 2011. A Numerical Study of Microscale Flow Behavior in Tight Gas and Shale Gas Reservoir Systems. Transport in Porous Media, 90(1): 253-268.

Frielinghaus, H., Feoktystov, A., Berts, I. and Mangiapia, G., 2015. KWS-1: Small-angle scattering diffractometer. Journal of large-scale research facilities, 1(A28).
Gaus, G., Amann-Hildenbrand, A., Krooss, B.M. and Fink, R., 2019. Gas permeability tests on core plugs from unconventional reservoir rocks under controlled stress: A comparison of different transient methods. Journal of Natural Gas Science and Engineering, 65: 224-236.
Gensterblum, Y., Ghanizadeh, A., Cuss, R.J., Amann-Hildenbrand, A., Krooss, B.M., Clarkson, C.R., Harrington, J.F. and Zoback, M.D., 2015. Gas transport and storage capacity in shale gas reservoirs – A review. Part A: Transport processes. Journal of Unconventional Oil and Gas Resources, 12: 87-122.
Ghanbarian, B., Hunt, A.G., Ewing, R.P. and Sahimi, M., 2013. Tortuosity in Porous Media: A Critical Review. Soil Science Society of America Journal, 77(5): 1461-1477.
Ghanizadeh, A., Amann-Hildenbrand, A., Gasparik, M., Gensterblum, Y., Krooss, B.M. and Littke, R., 2014a. Experimental study of fluid transport processes in the matrix system of the European organic-rich shales: II. Posidonia Shale (Lower Toarcian, northern Germany). International Journal of Coal Geology, 123: 20-33.
Ghanizadeh, A., Gasparik, M., Amann-Hildenbrand, A., Gensterblum, Y. and Krooss, B.M., 2014b. Experimental study of fluid transport processes in the matrix system of the European organic-rich shales: I. Scandinavian Alum Shale. Marine and Petroleum Geology, 51: 79-99.
Gjelberg, J., Martinsen, O.J., Charnock, M., Møller, N. and Antonsen, P., 2005. The reservoir development of the Late Maastrichtian–Early Paleocene Ormen Lange gas field, Møre Basin, Mid-Norwegian Shelf. Geological Society, London, Petroleum Geology Conference series, 6(1): 1165-1184.
Hammes, U. and Frébourg, G., 2012. Haynesville and Bossier mudrocks: A facies and sequence stratigraphic investigation, East Texas and Louisiana, USA. Marine and Petroleum Geology, 31(1): 8-26.
Ilgen, A.G., Heath, J.E., Akkutlu, I.Y., Bryndzia, L.T., Cole, D.R., Kharaka, Y.K., Kneafsey, T.J., Milliken, K.L., Pyrak-Nolte, L.J. and Suarez-Rivera, R., 2017. Shales at all scales: Exploring coupled processes in mudrocks. Earth-Science Reviews, 166: 132-152.
Jacops, E., Aertsens, M., Maes, N., Bruggeman, C., Krooss, B.M., Amann-Hildenbrand, A., Swennen, R. and Littke, R., 2017. Interplay of molecular size and pore network geometry on the diffusion of dissolved gases and HTO in Boom Clay. Applied Geochemistry, 76: 182–195.
Jarvie, D.M., Ronald J. Hill, Tim E. Ruble and Pollastro, R.M., 2007. Unconventional shale-gas systems: The Mississippian Barnett Shale of north-central Texas as one model for thermogenic shale-gas assessment. American Association of Petroleum Geologists Bulletin, 91(4): 475-499.
Javadpour, F., 2009. Nanopores and Apparent Permeability of Gas Flow in Mudrocks (Shales and Siltstone). Journal of Canadian Petroleum Technology, 48(08): 16-21.
Javadpour, F., Fisher, D. and Unsworth, M., 2007. Nanoscale Gas Flow in Shale Gas Sediments. Journal of Canadian Petroleum Technology, 46(10): 7.
Johansen, T.E.S. and Fossen, H., 2008. Internal geometry of fault damage zones in interbedded siliciclastic sediments. Geological Society, London, Special Publications, 299(1): 35-56.
Kampman, N.J.S., 2011. Fluid-Rock Interactions in a Carbon Storage Site Analogue, Green River, Utah, University of Cambridge, UK.
Katz, A.J. and Thompson, A.H., 1985. Fractal Sandstone Pores: Implications for Conductivity and Pore Formation. Physical Review Letters, 54(12): 1325-1328.
Klaver, J., Desbois, G., Littke, R. and Urai, J.L., 2015. BIB-SEM characterization of pore space morphology and distribution in postmature to overmature samples from the Haynesville and Bossier Shales. Marine and Petroleum Geology, 59: 451-466.
Klaver, J.M., 2014. Pore space characterization of organic-rich shales using BIB-SEM.
Knudsen, M., 1909. Die Gesetze der Molekularströmung und der inneren Reibungsströmung der Gase durch Röhren. Annalen der Physik, 333(1): 75-130.
Koura, K. and Matsumoto, H., 1991. Variable soft sphere molecular model for inverse-power-law or Lennard-Jones potential. Physics of Fluids A: Fluid Dynamics, 3(10): 2459-2465.
Koura, K. and Matsumoto, H., 1992. Variable soft sphere molecular model for air species. Physics of Fluids A: Fluid Dynamics, 4(5): 1083-1085.
Krohn, C.E., 1988. Fractal measurements of sandstones, shales, and carbonates. Journal of Geophysical Research: Solid Earth, 93(B4): 3297-3305.
Kuila, U., McCarty, D.K., Derkowski, A., Fischer, T.B., Topór, T. and Prasad, M., 2014. Nano-scale texture and porosity of organic matter and clay minerals in organic-rich mudrocks. Fuel, 135: 359-373.

Leu, L., Georgiadis, A., Blunt, M.J., Busch, A., Bertier, P., Schweinar, K., Liebi, M., Menzel, A. and Ott, H., 2016. Multiscale Description of Shale Pore Systems by Scanning SAXS and WAXS Microscopy. Energy & Fuels, 30(12): 10282-10297.
Li, Q., He, Y.L., Tang, G.H. and Tao, W.Q., 2011. Lattice Boltzmann modeling of microchannel flows in the transition flow regime. Microfluidics and Nanofluidics, 10(3): 607-618.
Liu, J.G. and Nie, Y.F., 2001. Fractal Scaling of effective diffusion coefficient of solute in porous media. . Journal of Environmental Sciences, 13(2): 458-462.
Liu, K. and Ostadhassan, M., 2017. Multi-scale fractal analysis of pores in shale rocks. Journal of Applied Geophysics, 140: 1-10.
Loucks, R.G., Reed, R.M., Ruppel, S.C. and Hammes, U., 2012. Spectrum of pore types and networks in mudrocks and a descriptive classification for matrix-related mudrock pores. AAPG Bulletin, 96(6): 1071-1098.
Loucks, R.G., Reed, R.M., Ruppel, S.C. and Jarvie, D.M., 2009. Morphology, Genesis, and Distribution of Nanometer-Scale Pores in Siliceous Mudstones of the Mississippian Barnett Shale. Journal of Sedimentary Research, 79(12): 848-861.
Mazurek, M., Elie, M., Hurford, A., Leu, W. and Gautschi, A., 2002. Burial history of Opalinus clay, International meeting on clays in natural and engineered barriers for radioactive waste confinement, France.
Mehmani, A., Prodanović, M. and Javadpour, F., 2013. Multiscale, Multiphysics Network Modeling of Shale Matrix Gas Flows. Transport in Porous Media, 99(2): 377-390.
Melnichenko, Y.B., 2015. Small-Angle Scattering from Confined and Interfacial Fluids: Applications to Energy Storage and Environmental Science. Springer, TN, USA.
Miao, T., Yang, S., Long, Z. and Yu, B., 2015. Fractal analysis of permeability of dual-porosity media embedded with random fractures. International Journal of Heat and Mass Transfer, 88: 814-821.
Mildner, D.F.R. and Hall, P.L., 1986. Small-angle scattering from porous solids with fractal geometry. Journal of Physics D: Applied Physics, 19(8): 1535.
Moldrup, P., Olesen, T., Komatsu, T., Schjønning, P. and Rolston, D.E., 2001. Tortuosity, Diffusivity, and Permeability in the Soil Liquid and Gaseous Phases. Soil Science Society of America Journal, 65(3): 613-623.
Möller, N.K., Gjelberg, J.G., Martinsen, O., Charnock, M.A., Færseth, R.B., Sperrevik, S. and Cartwright, J.A., 2004. A geological model for the Ormen Lange hydrocarbon reservoir. Norsk Geologisk Tidsskrift, 84: 169-190.
Nelson, P.H., 2009. Pore-throat sizes in sandstones, tight sandstones, and shales. American Association of Petroleum Geologists Bulletin, 93(3): 329-340.
Olsen, P.E., Kent, D.V., Cornet, B., Witte, W.K. and Schlische, R.W., 1996. High-resolution stratigraphy of the Newark rift basin (early Mesozoic, eastern North America). Bulletin of the Geological Society of America, 108(1): 40-77.
Pearson, F.J., Arcos, D., Bath, A., Boisson, J.Y., Fernández, A.M. and Gäbler, H.E., 2003. Mont Terri project-Geochemistry of water in the Opalinus Clay Formation at the Mont Terri rock laboratory. Berichte des BWG. Serie Geologie, 5.
Pearson, K., 2012. Geologic models and evaluation of undiscovered conventional and continuous oil and gas resources—Upper Cretaceous Austin Chalk, U.S. Gulf Coast, U.S. Geological Survey, Virginia, USA.
Petrie, E.S., Evans, J.P. and Bauer, S.J., 2014. Failure of cap-rock seals as determined from mechanical stratigraphy, stress history, and tensile-failure analysis of exhumed analogs. AAPG Bulletin, 98(11): 2365-2389.
Pipich, V., 2006. QtiKWS: SANS Data Treatment Package. Jülich Centre for Neutron Science JCNS at FRM-2 reactor, Garching, Germany.
Pipich, V. and Fu, Z., 2015. KWS-3: Very small angle scattering diffractometer with focusing mirror. Journal of large-scale research facilities, 1(A31).
Radlinski, A.P., 2006. Small-Angle Neutron Scattering and the Microstructure of Rocks. Reviews in Mineralogy and Geochemistry, 63(1): 363-397.
Radlinski, A.P., Boreham, C.J., Wignall, G.D. and Lin, J.S., 1996. Microstructural evolution of source rocks during hydrocarbon generation: A small-angle-scattering study. Physical Review B, 53(21): 14152-14160.
Rezaeyan, A., 2021. Using Small Angle Neutron Scattering (SANS) for a Systematic Understanding of the Pore Structure of Mudrocks of Different Origin. Monograph Thesis, Heriot-Watt University, Edinburgh, 213 pp.
Rezaeyan, A., Pipich, V., Bertier, P., Seemann, T., Leu, L., Kampman, N., Feoktystov, A., Barnsley, L.C. and Busch, A., 2019a. Microstructural Investigation of Mudrock Seals Using Nanometer-Scale Resolution Techniques, Sixth EAGE Shale Workshop. EAGE, Bordeaux, France.

Rezaeyan, A., Pipich, V., Bertier, P., Seemann, T., Leu, L., Kampman, N., Feoktystov, A., Barnsley, L.C. and Busch, A., 2019b. Quantitative Analysis of the Pore Structure of Premature-To-Postmature Organic Rich Mudrocks Using Small Angle Neutron Scattering, Sixth EAGE Shale Workshop. EAGE, Bordeaux, France.

Rezaeyan, A., Pipich, V. and Busch, A., 2021. MATSAS: A Small Angle Scattering Computer Tool for Porous Systems. Journal of Applied Crystallography, 54.

Rezaeyan, A., Seemann, T., Bertier, P., Pipich, V., Leu, L., Kampman, N., Feoktystov, A., Barnsley, L. and Busch, A., 2019c. Understanding Pore Structure of Mudrocks and Pore-Size Dependent Sorption Mechanism Using Small Angle Neutron Scattering, SPE/AAPG/SEG Asia Pacific Unconventional Resources Technology Conference. Unconventional Resources Technology Conference, Brisbane, Australia, pp. 13.

Ross, D.J.K. and Bustin, R.M., 2008. Characterizing the shale gas resource potential of Devonian–Mississippian strata in the Western Canada sedimentary basin: application of an integrated formation evaluation. AAPG Bulletin, 92(1): 87–125.

Rother, G., Melnichenko, Y.B., Cole, D.R., Frielinghaus, H. and Wignall, G.D., 2007. Microstructural Characterization of Adsorption and Depletion Regimes of Supercritical Fluids in Nanopores. The Journal of Physical Chemistry C, 111(43): 15736-15742.

Rother, G., Vlcek, L., Gruszkiewicz, M.S., Chialvo, A.A., Anovitz, L.M., BaÃ±uelos, J.L., Wallacher, D., Grimm, N. and Cole, D.R., 2014. Sorption Phase of Supercritical CO2 in Silica Aerogel: Experiments and Mesoscale Computer Simulations. The Journal of Physical Chemistry C, 118(28): 15525-15533.

Rutter, E.H., Mecklenburgh, J. and Taylor, K.G., 2017. Geomechanical and petrophysical properties of mudrocks: introduction. The Geological Society of London: Special Publications, 454(1): 1-13.

Sakhaee-Pour, A. and Bryant, S., 2012. Gas Permeability of Shale. SPE Reservoir Evaluation & Engineering, 15(04): 401-409.

Schlosser, J., Grathoff, G.H., Ostertag-Henning, C., Kaufhold, S. and Warr, L.N., 2016. Mineralogical changes in organic-rich Posidonia Shale during natural and experimental maturation. International Journal of Coal Geology, 157: 74-83.

Seemann, T., Bertier, P., Maes, N., Rezaeyan, A., Pipich, V., Barnsley, L., Busch, A. and Cnudde, V., 2019. Resolving the Pore Structure and Sorption Properties of Methane in Mudrocks - A Small Angle Neutron Scattering Study. 2019(1): 1-5.

Sellin, P. and Leupin, O.X., 2013. The Use Of Clay As An Engineered Barrier In Radioactive-Waste Management – A Review. Clays and Clay Minerals, 61(6): 477-498.

Sheng, M., Li, G., Tian, S., Huang, Z. and Chen, L., 2016. A Fractal Permeability Model For Shale Matrix With Multi-Scale Porous Structure. Fractals, 24(01): 1650002.

Sing, K.S.W., Everett, D.H., Haul, R.A.W., Moscou, L., Pierotti, R.A., Rouquerol, J. and Siemienewska, T., 1985. Reporting physisorption data for gas/solid systems with special reference to the determination of surface area and porosity. Pure and Applied Chemistry, 57(4): 603-619.

Tartakovsky, D.M. and Dentz, M., 2019. Diffusion in Porous Media: Phenomena and Mechanisms. Transport in Porous Media, 130(1): 105-127.

Teixeira, J., 1988. Small-angle scattering by fractal systems. Journal of Applied Crystallography, 21(6): 781-785.

Uffmann, A.K., Littke, R. and Rippen, D., 2012. Mineralogy and geochemistry of Mississippian and Lower Pennsylvanian Black Shales at the Northern Margin of the Variscan Mountain Belt (Germany and Belgium). International Journal of Coal Geology, 103: 92-108.

Vandenberghe, N., Craen, M.D. and Wouters, L., 2014. The Boom Clay Geology From sedimentation to present-day occurrence: A review, Royal Belgian Institute Of Natural Sciences, Belgium.

Vandewijngaerde, W., Piessens, K., Dusar, M., Bertier, P., Krooss, B.M., Littke, R. and Swennen, R., 2016. Investigations on the shale oil and gas potential of Westphalian mudstone successions in the Campine Basin, NE Belgium (well KB174): Palaeoenvironmental and palaeogeographical controls. Geologica Belgica, 19(3-4): 1-30.

Wang, F., Jiao, L., Lian, P. and Zeng, J., 2019. Apparent gas permeability, intrinsic permeability and liquid permeability of fractal porous media: Carbonate rock study with experiments and mathematical modelling. Journal of Petroleum Science and Engineering, 173: 1304-1315.

Wheatcraft, S.W. and Tyler, S.W., 1988. An explanation of scale-dependent dispersivity in heterogeneous aquifers using concepts of fractal geometry. Water Resources Research, 24(4): 566-578.

Wong, P.-z., Howard, J. and Lin, J.-S., 1986. Surface Roughening and the Fractal Nature of Rocks. Phys. Rev. Lett., 57: 637.

Wu, J. and Yu, B., 2007. A fractal resistance model for flow through porous media. International Journal of Heat and Mass Transfer, 50(19): 3925-3932.
Xiao, B., Fan, J. and Ding, F., 2014. A fractal analytical model for the permeabilities of fibrous gas diffusion layer in proton exchange membrane fuel cells. Electrochimica Acta, 134: 222-231.
Xu, P. and Yu, B., 2008. Developing a new form of permeability and Kozeny–Carman constant for homogeneous porous media by means of fractal geometry. Advances in Water Resources, 31(1): 74-81.
Yu, B. and Cheng, P., 2002. A fractal permeability model for bi-dispersed porous media. International Journal of Heat and Mass Transfer, 45(14): 2983-2993.
Yu, B. and Li, J., 2001. some fractal characters of porous media. Fractals, 09(03): 365-372.
Zhang, R., Liu, S. and Wang, Y., 2017. Fractal evolution under in situ pressure and sorption conditions for coal and shale. Scientific Reports, 7: 8971.
Zhang, T., Dong, M. and Li, Y., 2018. A Fractal Permeability Model for Shale Oil Reservoir. IOP Conference Series: Earth and Environmental Science, 108: 032083.
Zhang, Y.-H., Gu, X.-J., Barber, R.W. and Emerson, D.R., 2006. Capturing Knudsen layer phenomena using a lattice Boltzmann model. Physical Review E, 74(4): 046704.
Zhao, C., Hobbs, B.E. and Mühlhaus, H.B., 1998. Analysis of pore-fluid pressure gradient and effective vertical-stress gradient distribution in layered hydrodynamic systems. Geophysical Journal International, 134(2): 519-526.
Zheng, Q., Fan, J. and Xu, C., 2018. Fractal Model of Gas Diffusion through Porous Fibrous Materials with Rough Surfaces. Fractals, 26(05): 1850065.